AGU PUBLICATIONS

JGR

Journal of Geophysical Research: Oceans

RESEARCH ARTICLE

10.1002/2017JC012962

Subglacial discharge-driven renewal of tidewater glacier fjords

Dustin Carroll[1], David A. Sutherland[1], Emily L. Shroyer[2], Jonathan D. Nash[2], Ginny A. Catania[3,4], and Leigh A. Stearns[5]

[1]Department of Earth Sciences, University of Oregon, Eugene, Oregon, USA, [2]College of Earth, Ocean and Atmospheric Sciences, Oregon State University, Corvallis, Oregon, USA, [3]Department of Geological Sciences, University of Texas at Austin, Austin, Texas, USA, [4]Institute for Geophysics, University of Texas at Austin, Austin, Texas, USA, [5]Department of Geology, University of Kansas, Lawrence, Kansas, USA

Key Points:
- Glaciers grounded below the sill depth can renew fjord basins with subglacial discharge
- Wide fjords exhibit recirculation that increases dilution and residence time of glacially-modified waters
- Tide-sill interactions increase subglacial discharge-driven transport of deep shelf waters into fjord basins

Supporting Information:
- Supporting Information S1
- Movie S1
- Movie S2

Correspondence to:
D. Carroll,
dcarroll@uoregon.edu

Citation:
Carroll, D., D. A. Sutherland, E. L. Shroyer, J. D. Nash, G. A. Catania, and L. A. Stearns (2017), Subglacial discharge-driven renewal of tidewater glacier fjords, *J. Geophys. Res. Oceans*, *122*, 6611–6629, doi:10.1002/2017JC012962.

Received 4 APR 2017
Accepted 11 JUL 2017
Accepted article online 24 JUL 2017
Published online 24 AUG 2017

Abstract The classic model of fjord renewal is complicated by tidewater glacier fjords, where submarine melt and subglacial discharge provide substantial buoyancy forcing at depth. Here we use a suite of idealized, high-resolution numerical ocean simulations to investigate how fjord circulation driven by subglacial plumes, tides, and wind stress depends on fjord width, grounding line depth, and sill height. We find that the depth of the grounding line compared to the sill is a primary control on plume-driven renewal of basin waters. In wide fjords the plume exhibits strong lateral recirculation, increasing the dilution and residence time of glacially-modified waters. Rapid drawdown of basin waters by the subglacial plume in narrow fjords allows for shelf waters to cascade deep into the basin; wide fjords result in a thin, boundary current of shelf waters that flow toward the terminus slightly below sill depth. Wind forcing amplifies the plume-driven exchange flow; however, wind-induced vertical mixing is limited to near-surface waters. Tidal mixing over the sill increases in-fjord transport of deep shelf waters and erodes basin stratification above the sill depth. These results underscore the first-order importances of fjord-glacier geometry in controlling circulation in tidewater glacier fjords and, thus, ocean heat transport to the ice.

1. Introduction

Fjords act as deep, highly-stratified estuaries [*Geyer and Ralston*, 2011], with potential for continuous exchange between the fjord and adjacent coastal waters. In the classic model of fjord circulation [*Farmer and Freeland*, 1983], freshwater input at the head of the fjord, along with down-fjord wind stress [*Svendsen and Thompson*, 1978], drives a brackish outflow in the surface layer. Shear-driven entrainment in the outflow results in a compensating up-fjord flow of seawater to balance the loss of salt and mass. For fjords constrained by a shallow sill at the mouth, stratification below the brackish outflow consists of intermediary waters at the sill level, with deep basin waters found at depth [*Stigebrandt*, 2012].

In typical fjords, the width of the mouth and the sill depth act as first-order controls on fjord-shelf exchange. In narrow (i.e., nonrotating), shallow-silled fjords, exchange is typically regulated by hydraulic control [*Farmer and Denton*, 1985]. For fjords with wider mouths, and or, deeper sills, exchange above the sill level can be driven by fjord-shelf density gradients [*Aure and Stigebrandt*, 1990; *Aure et al.*, 1996; *Arneborg et al.*, 2004], resulting in a baroclinic "intermediary circulation" that is gradually damped as it propagates up-fjord. Additionally, the presence of a strong geostrophic coastal current can act to restrict exchange [*Klinck et al.*, 1981], which can isolate intermediary waters [*Svendsen et al.*, 2002; *Cottier et al.*, 2005; *Nilsen et al.*, 2008]. Previous work has shown that renewal of waters below sill depth is driven primarily by two processes: (1) high-density waters sink and replace the existing basin waters [*Geyer and Cannon*, 1982; *Stigebrandt*, 1987], and (2) diapycnal mixing [*Stigebrandt and Aure*, 1989]. Tidal flow over steep sill topography provides an important mechanism for transferring energy from barotropic to baroclinic processes [*Inall et al.*, 2004] and henceforth to turbulence and mixing. Supercritical tidal flow can produce jets [*Stashchuk et al.*, 2007], bores, and hydraulic jumps [*Staalstrøm et al.*, 2015] that elevate local turbulence near the sill; subcritical tidal flow can generate internal tides that radiate into the fjord and induce remote mixing [*Arneborg and Liljebladh*, 2009].

This paradigm of fjord circulation and renewal provides valuable insight into many fjord systems; however, it is complicated by tidewater glacier fjords, where submarine melt of the terminus [*Slater et al.*, 2015] and

icebergs [*Enderlin et al.*, 2016] and subglacial discharge [*Chauché et al.*, 2014; *Carroll et al.*, 2015, 2016; *Stevens et al.*, 2016; *Mankoff et al.*, 2016] can provide substantial buoyancy forcing at depth [*Straneo et al.*, 2011; *Jackson and Straneo*, 2016]. Tidewater glacier fjords provide a critical pathway by which glacially-modified waters are discharged to the coastal ocean [*Bamber et al.*, 2012] and warm ocean waters are transmitted to ice sheet margins [*Straneo and Heimbach*, 2013]. Recent dynamic mass loss from the Greenland Ice Sheet [*van den Broeke et al.*, 2009; *Enderlin et al.*, 2014], which is driven by frontal ablation (calving and submarine melt) of tidewater glacier termini, has motivated numerous observational studies of hydrography and circulation in Greenland fjords (for a review, see *Straneo and Cenedese* [2015]).

However, we still lack a precise understanding of how circulation in tidewater glacier fjords is modulated by fjord-glacier geometry (i.e., fjord width, topographic constrictions, and glacier depth) [*Beaird et al.*, 2015; *Rignot et al.*, 2016], due to a lack of sustained, full-depth ocean measurements across various Greenland fjords. Although observations are sparse, progress has been made on characterizing fjord circulation using numerical ocean models [*Cowton et al.*, 2015; *Carroll et al.*, 2015]. While these previous modeling efforts have been useful, they are two-dimensional [*Sciascia et al.*, 2014; *Gladish et al.*, 2015], focus on systems without sills [*Cowton et al.*, 2016], neglect tidal forcing, and often lack the horizontal resolution [*Bendtsen et al.*, 2015] to resolve cross-fjord gradients in the exchange flow.

Here we use a suite of idealized high-resolution ocean simulations to systematically evaluate how subglacial discharge-driven exchange flow and renewal of basin waters is influenced by fjord, sill, and glacier geometry. Additionally, we include simulations with tides and wind stress to determine how external forcing modulates the background exchange flow. While our model is idealized and neglects additional sources of buoyancy such as terrestrial runoff and sea ice/iceberg melt, our results provide valuable insight for future parameterizations of tidewater glacier fjords in large-scale climate models. This work demonstrates that subglacial discharge emerging from glaciers grounded below the sill depth can draw shelf waters over a sill and into fjord basins, providing an ice-sheet forced mechanism for seasonal renewal that occurs independently of external shelf forcing.

2. Model Setup

2.1. MITgcm Configuration

To investigate the sensitivity of tidewater glacier fjord circulation to variations in forcing and fjord-glacier geometry (Table 1), we use the Massachusetts Institute of Technology general circulation model (MITgcm) in a three-dimensional, hydrostatic configuration. The MITgcm is a developed version of *Marshall et al.* [1997], which integrates the primitive Boussinesq equations on a Arakawa staggered C-grid [*Arakawa and*

Table 1. List of MITgcm Simulations[a]

Simulation Name	W (km)	H_s/H	H_{gl}/H	Q_{sg} ($m^3\ s^{-1}$)	Tides	τ_x/Duration ($N\ m^{-2}$/d)	τ_y/Duration ($N\ m^{-2}$/d)	# of Simulations
Vertical Plume Only Runs								
plumeShallowSill	2, 5, 10, 20	0.1	1	50, 250	No	0	0	8
plumeW2	2	0.25, 0.5, 1	0.25, 0.5, 1	250	No	0	0	9
plumeW5	5	0.25, 0.5, 1	0.25, 0.5, 1	250	No	0	0	9
plumeW10	10	0.25, 0.5, 1	0.25, 0.5, 1	250	No	0	0	9
plumeW20	20	0.25, 0.5, 1	0.25, 0.5, 1	250	No	0	0	9
Tide runs								
tideOnly	2, 5, 10, 20	0.25, 0.5, 1	0.25	0	Yes	0	0	12
plumeTide	2, 5, 10, 20	0.25	0.25, 0.5, 1	250	Yes	0	0	12
plumeTideNoSill	2, 5, 10, 20	1	0.25	250	Yes	0	0	4
Wind runs								
zonalWind3Day	2, 10	0.25	0.25	0	No	−0.4/3	0	2
meridWind3Day	2, 10	0.25	0.25	0	No	0	−0.4/3	2
plumeZonalWind3Day	2, 10	0.25	0.25, 0.5, 1	250	No	−0.4/3	0	6
plumeMeridWind3Day	2, 10	0.25	0.25, 0.5, 1	250	No	0	−0.4/3	6
plumeZonalWind3DayNoSill	2, 10	1	0.25	250	No	−0.4/3	0	2
plumeMeridWind3DayNoSill	2, 10	1	0.25	250	No	0	−0.4/3	2
plumeZonalWind12Day	2, 10	0.25	0.25	250	No	−0.4/12	0	2
plumeMeridWind12Day	2, 10	0.25	0.25	250	No	0	−0.4/12	2

[a]See section 2 for details, 96 simulations total.

Lamb, 1977]. The fjord is represented as a 60 km long channel, with width W and maximum basin depth H of 800 m (Figures 1a and 1b). The glacier terminus is treated as a vertical wall at the fjord head, grounded at depth H_{gl}. The western portion of the model domain contains a uniform shelf with a width of 65 km and depth of 800 m. The model domain is treated as an f-plane with a nonlinear free surface. No-slip conditions are enforced at solid boundaries, with drag parameterized by a quadratic drag law coefficient C_D of 2.5×10^{-3}. The fjord mouth contains a topographic sill (Figure 1b), with the analytic form

$$h(x) = -H + (H_s - H)\ \exp\left[-\frac{x^2}{2L^2}\right], \tag{1}$$

where H_s is the sill depth, and L is the width of the slope (L is set to 5 km in all simulations). The horizontal grid resolution (Δx, Δy) is 200 m inside the fjord, linearly telescoping to 2 km at open boundaries on the shelf. Vertical resolution (Δz) ranges from 10 m at the free surface to a maximum of 50 m at depth. The vertical and horizontal resolution at the sill crest is 20 m and 200 m, respectively; partial grid cells are used represent the steep-sided sill topography, with a minimum nondimensional fraction of 0.2 [*Adcroft et al*., 1997]. The total number of grid cells, $nx \times ny \times nz$, is $360 \times 270 \times 38$.

Initial temperature and salinity fields are prescribed from mean 2014 summer hydrographic observations from Rink fjord, west Greenland [*Bartholomaus et al*., 2016]. Stratification in Rink fjord is typical of deep

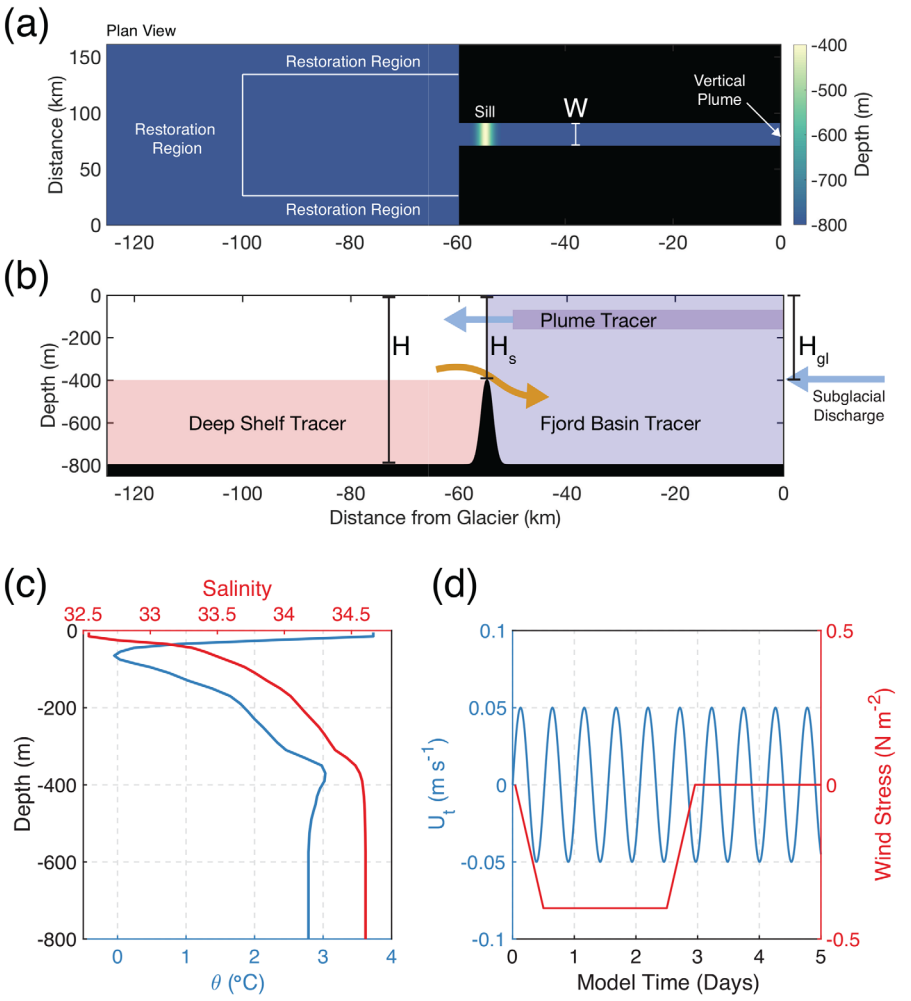

Figure 1. MITgcm model domain and forcing. (a) plan view of model domain ($W = 20$ km, $H_s/H = 0.5$, and $H_{gl}/H = 0.5$ case is shown); vertical plume is located at the centerline of the fjord head (x = 0 km, y = 80 km). (b) Centerline fjord bathymetry and passive tracers used in this study. (c) Initial model potential temperature and salinity profiles from Rink fjord, west Greenland. (d) Idealized tidal and wind stress forcing.

Greenland fjords, consisting of warm salty Atlantic-origin water at depth overlain by cold, fresh polar water and a seasonal layer of warm surface water (Figure 1c). The mode-1 internal wave phase speed computed from initial model hydrography is $\sim$0.8 m s^{-1}, corresponding to an internal deformation radius L_R of $\sim$6 km for the latitude simulated (70°, $f = 1.367$ s^{-1}). We note that simulations with shallow sills can locally reduce the initial deformation radius in the basin (where $H = -800$ m) by roughly a factor of two, due to destratification of ambient waters by sill-driven mixing. The equation of state (JMD95Z) follows *Jackett and Mcdougall* [1995]. The shelf region contains open boundaries at the north, south, and west edges; temperature and salinity at the boundaries are restored to prescribed initial conditions. Each open boundary contains a 20 km restoration region to prevent internal waves from reflecting back into the fjord, with an inner (outer) relaxation timescale of 1 h (1 day). We use an adaptive grid-scaled Laplacian horizontal viscosity in order to maintain a grid-scale Reynolds number that is $\mathcal{O}(1)$; a horizontal biharmonic viscosity of 10^{-3} m^4 s^{-1} is used to suppress grid-scale noise. Vertical mixing is parameterized using the nonlocal K-Profile Parameterization (KPP) scheme [*Large et al*., 1994], with a background viscosity set to 10^{-5} m^2 s^{-1}. A third order, direct-space-time flux-limited advection scheme (MITgcm tracer advection option 33) is used to eliminate extrema in the tracer field; explicit diffusivities for temperature, salinity, and passive tracers are set to zero.

Passive tracers, initialized with a concentration of unity, are injected into deep shelf waters (referred henceforth as Deep Shelf Tracer (DST)), fjord basin, and subglacial plume waters to visualize flow and estimate renewal timescales (Figure 1b). DST is injected into shelf waters to the left of the sill crest ($x < -55$ km) and from the sill level to bottom depth ($z = -800$ m); fjord basin tracer is injected into fjord waters to the right of the sill crest ($x > -55$ km) over the entire water column. DST concentrations to the left of the sill crest are continually relaxed toward unity with a relaxation timescale of 1 h. We use neutrally-buoyant Lagrangian floats (MITgcm FLT package) initialized at the fjord mouth and near-glacier region to visualize particle trajectories and estimate mean properties in the plume and deep return flow toward the glacier. Three-dimensional float trajectories and tracer properties are integrated hourly with a fourth-order Runge-Kutta scheme; velocities and positions are bilinearly interpolated between grid cells.

2.2. Subglacial Plume Forcing

The fjord-scale model described in this study lacks the grid resolution to resolve nonhydrostatic plume dynamics at the glacier terminus [*Xu et al*., 2012, 2013; *Sciascia et al*., 2013; *Slater et al*., 2015; *Carroll et al*., 2015]. Therefore, we use a theoretical plume model [*Morton et al*., 1956; *Jenkins*, 2011] coupled to the MITgcm [*Cowton et al*., 2015] to parameterize vertical convection in a half-conical, point source vertical plume adjacent to the glacier terminus. For the remainder of the paper, we use the term "vertical plume" to describe the parameterized convective plume adjacent to the glacier terminus and "plume" to describe the resultant out-fjord buoyancy-driven current. At each grid cell where the vertical plume is entraining, ambient fluid and tracers are removed, diluted according to plume theory, and placed into the cell where the vertical plume reaches neutral buoyancy (i.e., the terminal level). The vertical plume is located at the glacier centerline ($y = 80$ km); the initial subglacial discharge flux (Q_{sg}) is held constant during each individual model run. Mass is conserved in the vertical plume, which results in a small decrease ($< 2\%$) in volume flux at the neutral buoyancy depth. Submarine melt in the vertical plume is calculated using the three-equation formulation of *Holland and Jenkins* [1999]; cooling and freshening of adjacent grid cells is implemented as a virtual salt and heat flux [*Huang*, 1993]. For a terminus depth of 800 m and width of 10 km, including ambient melt outside of the plume region [*Cowton et al*., 2015] results in a $<1\%$ increase in exchange-flow transport and a slight cooling and freshening of fjord waters, therefore we neglect ambient melt. Simulations with vertical plume forcing only are run for 120 days (Table 1, blue cells).

2.3. Tidal and Wind Forcing

Tidal forcing $U_t = U_0 \sin(\omega t)$ is applied as a uniform, barotropic zonal velocity at the M2 tidal frequency ($\omega = 1.4 \times 10^{-4}$ s^{-1}) along the western boundary of the model domain (Figure 1d). The velocity amplitude U_0 is set to 5×10^{-2} m s^{-1}, typical of predicted Arctic Ocean inverse barotropic tidal model (AOTIM) velocities on the west Greenland shelf [*Padman and Erofeeva*, 2004]. Model output for tidal simulations is stored hourly, subtidal fields are generated with a Godin filter of consecutive 24–24-25 h moving averages [*Godin*, 1991]. Simulations with tidal forcing only and vertical plume and tidal forcing are run for 120 days (Table 1, green cells).

To investigate the response of the buoyancy-driven exchange flow to synoptic wind events, we force the model with negative along-shelf and along-fjord wind stress (down-coast and down-fjord winds, respectively). Wind stress is applied as a "top-hat" forcing, with a linear ramp-up and ramp-down period (Figure 1d). The forcing time (3 days) is the sum of the ramp-up (0.5 day) and ramp-down time (0.5 day), and the time in which the wind stress is held constant (2 days). We conduct simulations with single (1 top-hat, 3 days total) and repeated (4 consecutive top-hats, 12 days total) wind events. Maximum wind stress magnitude is set to 0.4 N m^{-2}, consistent with reanalysis of storm events on the southeast Greenland shelf [*Harden et al*., 2011; *Jackson et al*., 2014]. Along-shelf and along-fjord wind stress relax linearly to zero in a 12 km wide region adjacent to the fjord-shelf boundary. Wind stress is applied at the end of the subglacial plume simulations (day 120); the model is then run for an additional 40 days to examine the transient response of the fjord (Table 1, red cells).

3. Results

3.1. Base Case: Vertical Plume Forcing

3.1.1. Transient Evolution

We first examine the influence of grounding line depth on the transient evolution of the exchange flow in a rapidly rotating, mid-width fjord ($W = 10$ km) with no sill (Figures 2 and 3; Table 1, blue cells). Discharge emerging from a shallow grounding line ($H_{gl}/H = 0.25$) produces a cold, fresh surface-confined plume (Figure 2 and supporting information Figure S1). During the initial model state the near-glacier plume develops into an anticyclonic bolus with a cyclonic return flow at depth (Figure 2a). Down-fjord from the glacier, a thin outflowing boundary current grows uniformly in the cross-fjord direction along the north wall. The near-glacier plume has a maximum velocity of 0.45 m s^{-1}, with minimum potential temperature and salinity anomalies of -2.68°C and -2.10, respectively. At day 9, an anticyclonic vortex detaches from the near-glacier bolus and begins to propagate down-fjord (Figure 2b). In the outflowing boundary current, unstable waves develop with a wavelength of ~10 km and maximum amplitude of ~5 km. By day 18 and thereafter, wave patterns become obscure and salinity gradients begin to weaken (Figure 2c). We note that model

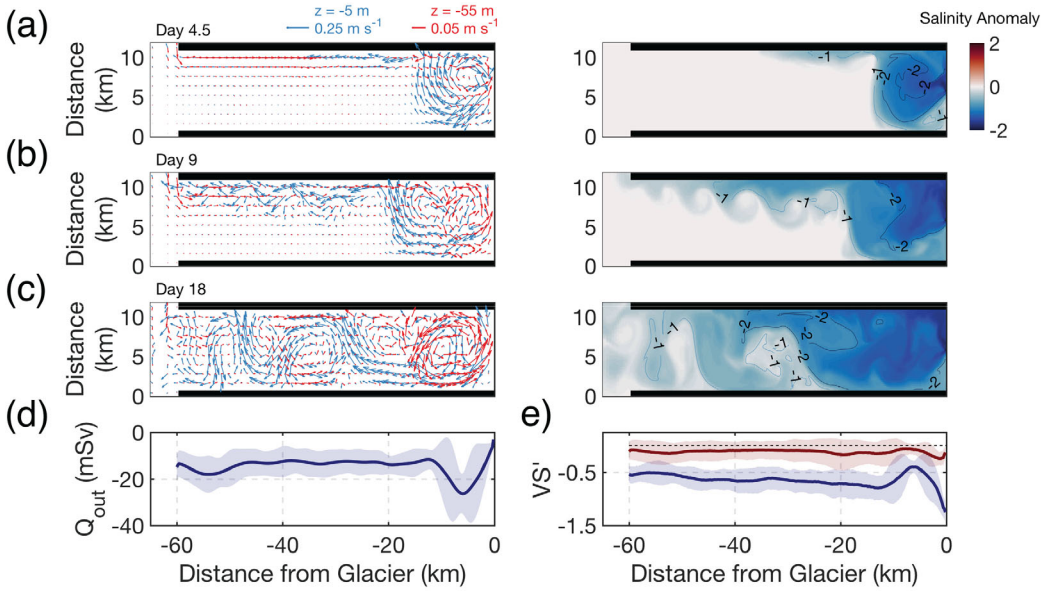

Figure 2. Transient evolution of the exchange flow at day (a) 4.5, (b) day 9, and (c) day 18 for a shallow grounding line with no sill ($H_{gl}/H = 0.25$, $H_s/H = 1$). Fjord width is 10 km; subglacial discharge flux is 250 m^3 s^{-1}. Blue and red arrows show velocity vectors in the plume and return flow ($z = -5$ m and $z = -55$ m), respectively. Shaded and black contours represent salinity and potential temperature anomalies at the plume depth ($z = -5$ m), respectively; anomalies are taken with respect to initial model conditions. (d) Out-fjord volume transport as a function of distance from glacier. (e) Out-fjord (blue) and in-fjord (red) volume-weighted salinity anomaly (VS') as a function of distance from glacier. Volume transports and volume-weighted salinity anomalies are averaged over day 30–120; shaded error bars show temporal variability in the exchange flow (two standard deviations).

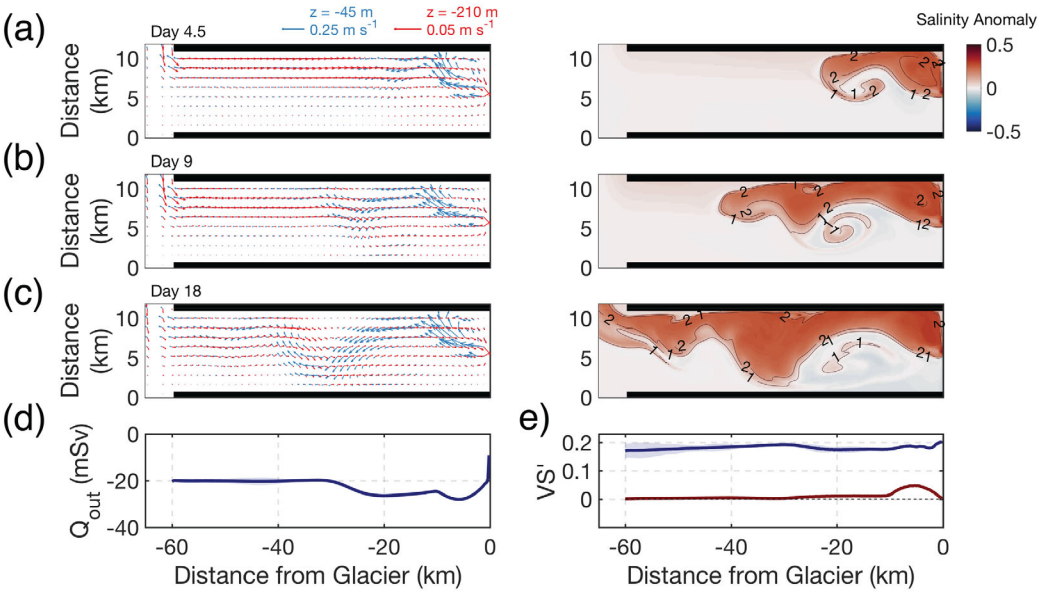

Figure 3. Transient evolution of the exchange flow at (a) day 4.5, (b) day 9, and (c) day 18 for a deep grounding line with no sill ($H_{gl}/H = 1$, $H_s/H = 1$). Fjord width is 10 km; subglacial discharge flux is 250 $m^3\ s^{-1}$. Blue and red arrows show velocity vectors in the plume and return flow ($z = -45$ m and $z = -210$ m), respectively. Shaded and black contours represent salinity and potential temperature anomalies at the plume depth ($z = -45$ m), respectively; anomalies are taken with respect to initial model conditions. (d) Out-fjord volume transport as a function of distance from glacier. (e) Out-fjord (blue) and in-fjord (red) volume-weighted salinity anomaly (VS') as a function of distance from glacier. Volume transports and volume-weighted salinity anomalies are averaged over day 30–120; shaded error bars show temporal variability in the exchange flow (two standard deviations).

spin-up time generally increases with fjord width, due to the influence of unsteady eddies and recirculation (supporting information Figure S2). We compute out- and in-fjord volume transports (Q_{out} and Q_{in}) as

$$Q_{out} = \int\int_A u_{out}\, dA\ , \tag{2}$$

$$Q_{in} = \int\int_A u_{in}\, dA\ , \tag{3}$$

where u_{out} and u_{in} are the out- and in-fjord velocities and A is the cross-sectional area of the fjord. Out-fjord volume transport increases most rapidly in the near-glacier region (-12 km $\leq x \leq 0$ km) due to vigorous lateral and vertical mixing of ambient waters into the plume (Figure 2d). For all plume simulations, net flow across open boundaries is balanced (i.e., $Q_{out} = Q_{in}$). Entrainment in the plume increases outflowing volume transport as the plume transits down-fjord, with a ~26% increase in Q_{out} from 12 km down-glacier to the fjord mouth. We emphasize that these results focus on the relative change between simulations; caution should be used in interpreting volume transport magnitudes as plume entrainment is dependent on the choice of model eddy viscosity/diffusivity. To estimate bulk tracer properties in the outflowing plume and return flow toward the glacier, we compute out- and in-fjord volume weighted salinity anomalies VS'_{out} and VS'_{in} as

$$VS'_{out} = \int\int_A u_{out}(S_{out} - S_0)\, dA \Big/ \int\int_A u_{out}\, dA\ , \tag{4}$$

$$VS'_{in} = \int\int_A u_{in}(S_{in} - S_0)\, dA \Big/ \int\int_A u_{in}\, dA\ , \tag{5}$$

where S_{out} and S_{in} are the out- and in-fjord salinity anomalies and S_0 is the initial model salinity profile (i.e., ambient conditions). The shallow grounding line results in a negative mean VS'_{out} that is diluted toward ambient fjord properties as the plume transits down-fjord (~44% increase from 12 km down-glacier to

mouth) (Figure 2e). Mean VS'_{in} is slightly negative at the mouth (–0.11), decreasing to −0.14 at 12 km down-glacier due to entrainment of fresh plume waters into the return flow beneath the plume.

In contrast, the deep grounding line ($H_{gl}/H = 1$) produces a vertical plume that entrains a larger percentage of Atlantic-origin water and reaches neutral buoyancy at depth in the cool, fresh polar water layer; this results in a warm, salty subsurface plume with maximum potential temperature and salinity anomalies at day 4 of 2.48°C and 0.37, respectively (Figure 3a and supporting information Figure S3). Similar to the shallow grounding line case, the near-glacier plume develops an anticyclonic rotation that is offset toward the north wall of the fjord, with a weak cyclonic return flow. By day 9, a southward flowing meander develops in the exchange flow approximately 25 km down-glacier (Figure 3b). At day 18 and thereafter, the meander develops into a quasi-steady feature located 30 km down-glacier, resulting in weak recirculation toward the glacier at the south wall (Figure 3c) that intensifies as the model reaches quasi-steady state. For equivalent subglacial discharge, the deep glacier results in larger out-fjord volume transport compared to the shallow glacier, due to increased entrainment of ambient waters in the coupled plume model (Figure 3d). Outflowing volume transport increases rapidly in the near-glacier field (maximum Q_{out} of −27.9 mSv at x = −5.8 km) and subsequently decreases toward the recirculation cell at x = −30 km (Figure 3d), indicative of along-fjord divergence in the flow. From the recirculation cell to the fjord mouth, outflowing volume transport increases by <1%. The deep grounding line results in a positive mean VS'_{out} of 0.19 at x = −5.8 km, decreasing to 0.17 at the fjord mouth due to dilution of the plume. Mean VS'_{in} is negligible at the fjord mouth (<0.15% increase from ambient conditions), reaching a maximum value of 0.05 at x = −5.5 km.

3.1.2. Along-Fjord Structure and Transport

We next examine how grounding line depth influences the along-fjord exchange flow structure and basin renewal (Figure 4). For weak subglacial discharge emerging from a deeply-grounded glacier, the presence of a shallow sill traps a weak outflowing plume in the fjord basin (peak along-fjord velocity of −0.01 m s^{-1} at z = −135 m), with a small overflow above the sill depth (Figure 4a). In systems with glaciers grounded above, and or, at sill depth, deep fjord waters remain isolated from the exchange flow (Figures 4b and 4c),

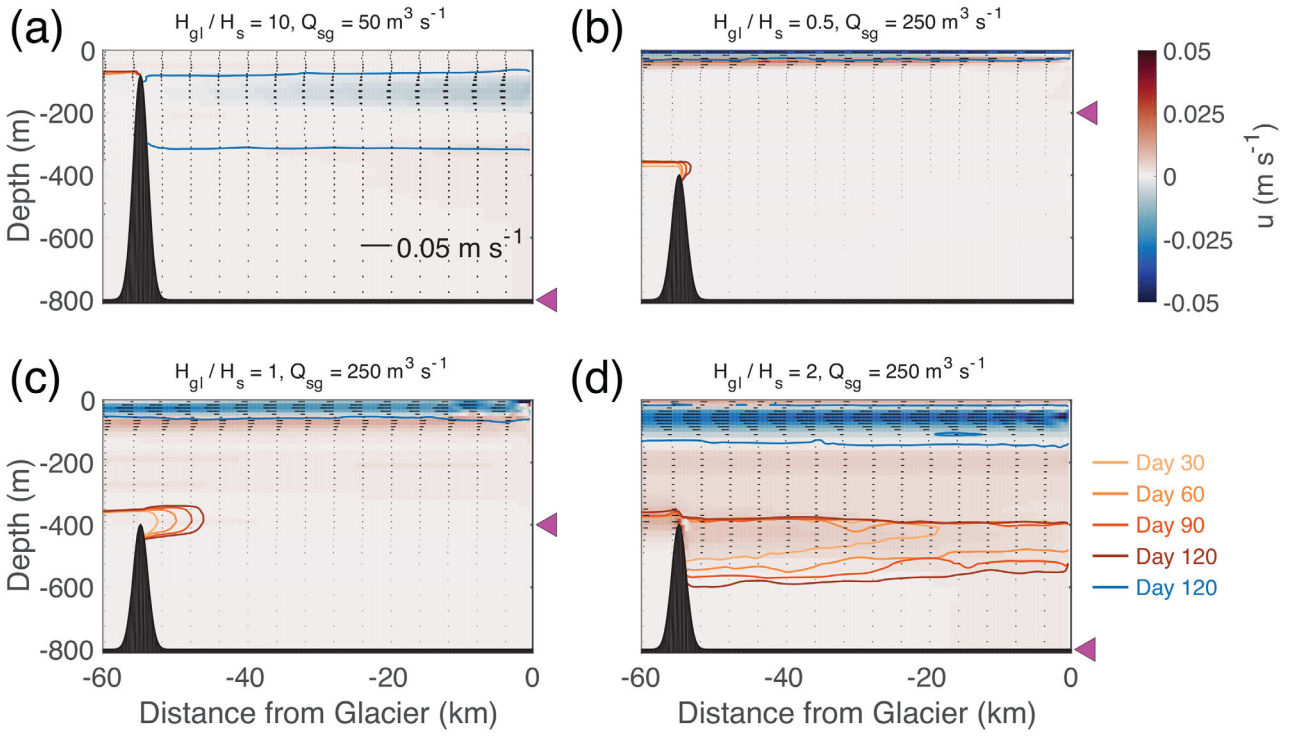

Figure 4. Along-fjord velocity and tracer evolution for varying sill-glacier geometry and subglacial discharge flux. Fjord width is 10 km. Shaded colors show mean along-fjord velocity; black arrows represent velocity vectors. Along-fjord velocity is averaged over model day 30–120; both velocity and tracers are averaged in the cross-fjord direction. Contours represent tracer concentrations of 0.1 for the plume at day 120 (blue) and deep shelf tracer at day 30, 60, 90, and 120 (orange to red colors). Left-pointing triangles represent grounding line depth.

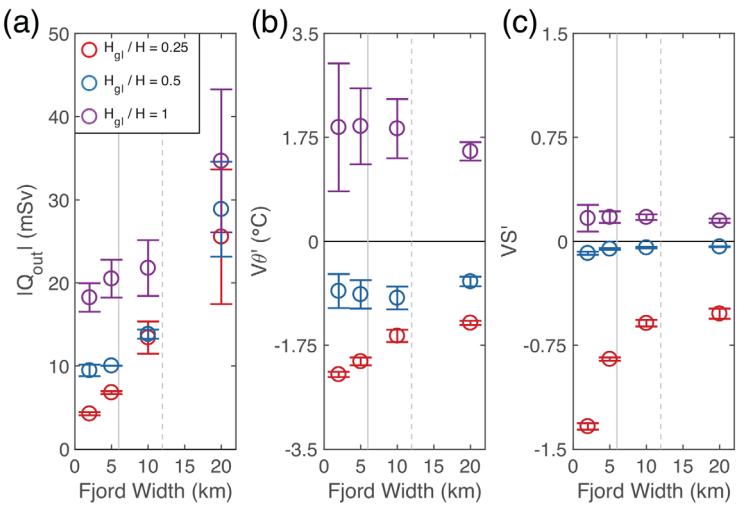

Figure 5. Out-fjord volume transport (a) and volume-weighted potential temperature (b) and salinity anomaly (c) computed at the fjord mouth (x = −60 km) for varying sill, fjord, and glacier geometry. Subglacial discharge flux is 250 m^3 s^{-1}. Colors show grounding line depth. Open circles represent mean values averaged over the range of sill depths and over day 90–120; error bars show two standard deviations from mean. Solid and dashed vertical lines show the internal deformation radius L_R and $2L_R$, respectively. L_R is computed from initial fjord hydrography. Note the different scales used on the *y* axis in Figures 5b and 5c.

inhibiting renewal of basin waters. For this glacier depth ($H_g/H \leq 0.5$) and subglacial discharge flux of 250 m^3 s^{-1}, the plume is confined to near-surface depths, with the strongest return flow in the shear layer directly beneath the outflow. For $H_g/H = 1$, the simulation results in a diffuse subsurface plume that spans ~120 m in the vertical, with a peak along-fjord velocity of −0.05 m s^{-1} at 55 m depth (Figure 4d). In this case, entrainment in the vertical plume exports deep basin waters to shallower depths, enabling the return flow to progressively fill the basin with a weakly-stratified layer fed by waters at the sill depth.

Increasing fjord width results in larger out-fjord volume transport, due to increased lateral and vertical mixing in the plume from recirculation (Figure 5a). This increase in out-fjord volume transport is accompanied by elevated variance in transport, due to temporal variability in the exchange flow driven by recirculation cells. For all fjord widths simulated, deep grounding lines result in the largest out-fjord volume transports due to increased entrainment in the vertical plume. Increased ambient mixing in wide fjords tends to relax out-fjord volume-weighted potential temperature and salinity anomalies toward ambient conditions (Figures 5b and 5c). Note that out-fjord volume-weighted potential temperature anomaly is computed in the same manner as equation (4). Plume dilution is most sensitive to fjord width in systems with shallow glaciers, where instability and recirculation in the exchange flow erodes and mixes strong near-surface stratification into the surface-confined plume.

3.1.3. Passive Tracers

To assess the influence of fjord-glacier geometry on renewal of basin waters we compute the fraction of fjord basin tracer and DST remaining in the basin at model day 120. Tracer fraction is computed by integrating tracer concentrations from the right of the sill crest to the first wet grid cell adjacent to the glacier wall (i.e., x = −55 km to x = −0.2 km) and normalizing by the basin volume over the same region. The fraction of basin tracer remaining at day 120 is most sensitive to grounding line and sill depth in narrow fjords, where the exchange flow-driven export of basin waters acts on a smaller basin volume (Figure 6a). For the narrowest fjord simulated (W = 2 km), a deep grounding line (purple markers) results in a drawdown of fjord basin tracer fraction below 0.3 for all sill depths tested. For a fjord width of 5 km, drawdown below this level only occurs when $H_s/H = 1$. The effect of the sill in limiting basin tracer export is most pronounced in deeply-grounded glaciers, where the deep return flow interacts with sill topography. For all cases, the addition of a shallow sill ($H_s/H = 0.1$) is roughly equivalent to reducing the grounding line depth by a factor of one half. Narrow fjords with deep grounding lines contain the largest fraction of DST in the basin at model day 120; in these simulations the vertical plume quickly draws down and fills the small basin volume with ambient waters at the sill depth (Figure 6b). Systems with shallow grounding lines ($H_g/H = 0.25$) result in negligible transport of DST into the basin (<0.01 for all fjord widths and sill depths tested). For deep grounding lines with shallow and mid-depth sills ($H_s/H = 0.25$ and 0.5), in-fjord transport is constrained through a smaller cross-sectional area, resulting in increased return flow velocities in the first wet cell above sill depth and elevated transport of DST into the basin. For the shallowest sill simulated ($H_s/H = 0.1$), sill topography partially blocks the exchange flow (not shown) and diminishes this effect.

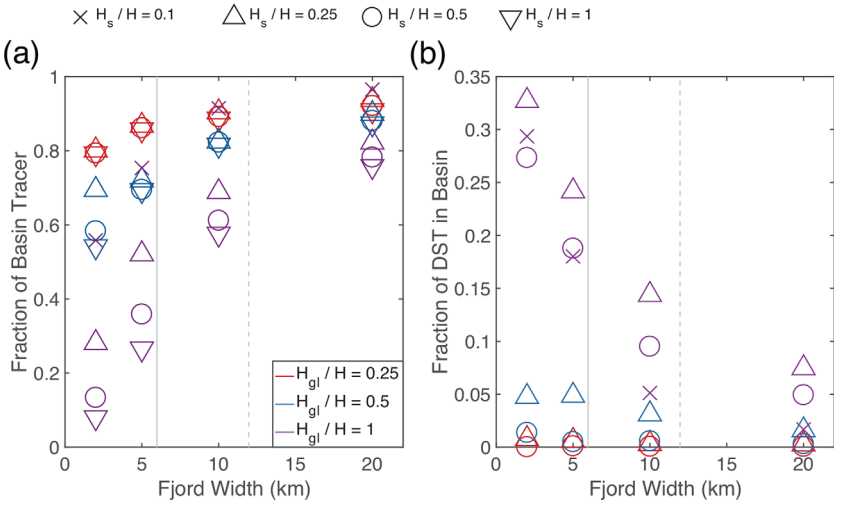

Figure 6. Fraction of (a) fjord basin tracer and DST tracer (b) in basin at model day 120 for varying sill, fjord, and glacier geometry. Subglacial discharge flux is 250 $m^3\ s^{-1}$. Marker shapes show sill depth; colors represent grounding line depth. Solid and dashed vertical lines show the internal deformation radius L_R and $2L_R$, respectively. L_R is computed from initial fjord hydrography.

3.1.4. Lagrangian Floats

In order to separate the exchange flow from coherent flow structures (such as recirculation cells and eddies) that persist in the fjord, we compute trajectories and statistical properties of time-released Lagrangian floats in the plume and deep return flow (Figures 7–9). For this section, we focus on the case where the glacier is grounded below the sill depth ($H_{gl}/H = 1$ and $H_s/H = 0.5$), generating a return flow that draws shelf waters at the sill depth into the fjord basin.

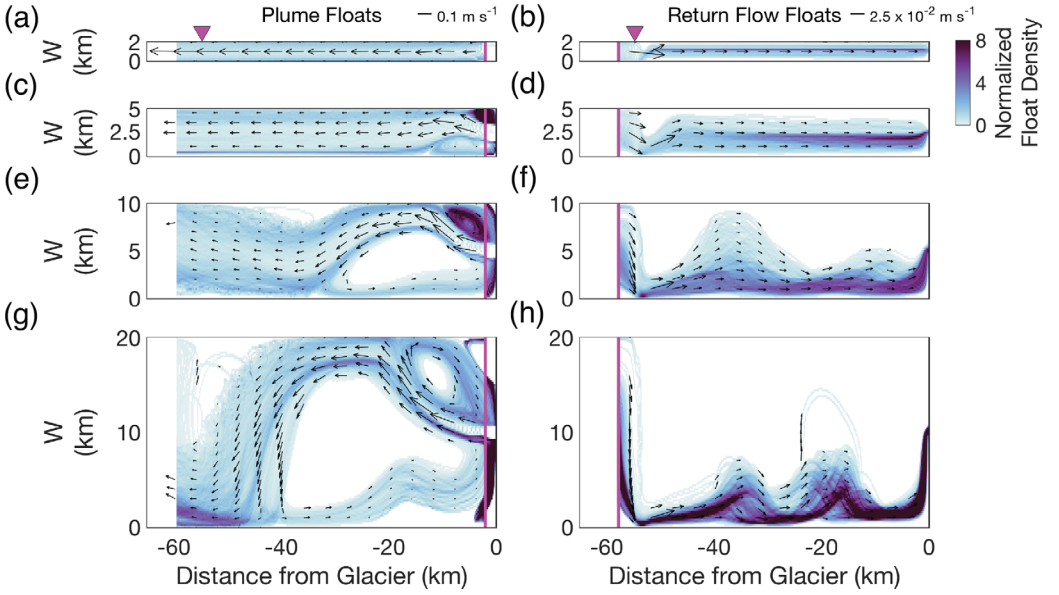

Figure 7. Normalized density for (a) plume and (b) return flow floats. Fjord width is varied from 2 to 20 km. Sill-glacier geometry corresponds to $H_s/H = 0.5$, $H_{gl}/H = 1$; subglacial discharge flux is 250 $m^3\ s^{-1}$. Plume and return flow floats spanning the width of the fjord are time-released daily from day 30 to 120 at near-glacier (x = −2 km; z = −45 m) and fjord mouth (x = −58 km; z = −390 m) locations, respectively. Dashed magenta line shows the along-fjord location of the float release; downward-pointing triangles show the location of the sill crest. Shaded colors represent integrated float density over the release duration, normalized by mean float density in the fjord. Black arrows show mean float velocity vectors, spaced at 1 km intervals in the cross-fjord direction. Float densities are computed from plume and return flow floats that successfully transit to the fjord mouth (x = −60 km) and first wet cell adjacent to the glacier (x = −0.2 km), respectively.

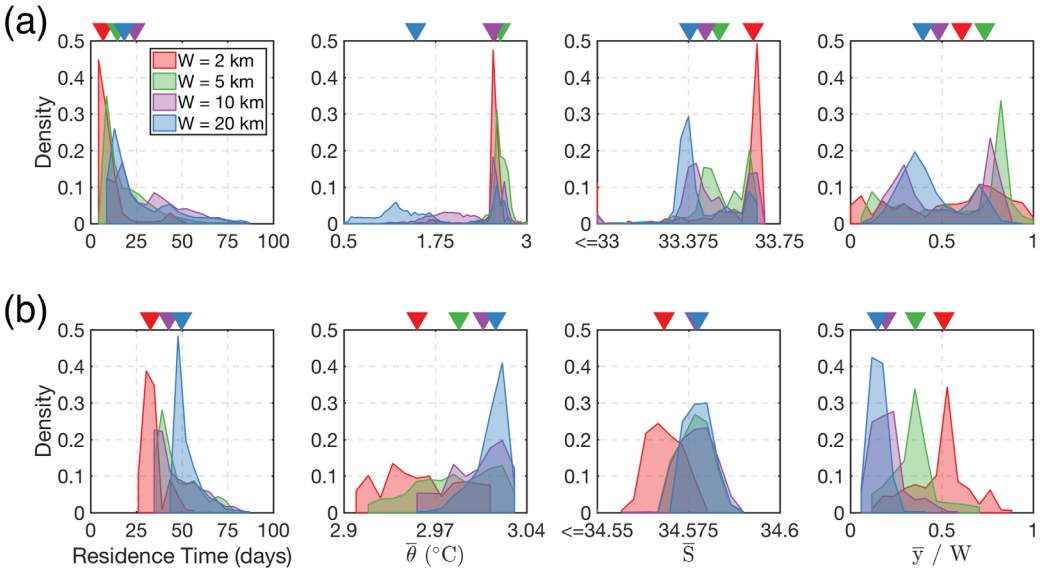

Figure 8. Normalized histogram of plume (a) and deep return float (b) residence time, potential temperature, salinity, and normalized cross-fjord position for varied fjord width. Sill-glacier geometry corresponds to $H_s/H = 0.5$, $H_{gl}/H = 1$; subglacial discharge flux is 250 $m^3\ s^{-1}$. Plume and return flow floats spanning the width of the fjord are time-released daily after day 30 at near-glacier (x = −2 km; z = −45 m) and fjord mouth (x = −58 km; z = −390 m) locations. Histograms are computed from mean plume and return flow float properties, averaged over the transit to the fjord mouth (x = −60 km) and first wet cell adjacent to the glacier (x = −0.2 km), respectively. Colors represent fjord width; downward-pointing triangles show median values.

The spatial distribution of plume and return flow floats reveals the complex circulation that results from interactions between the exchange flow and recirculation cells/eddies (Figures 7a–7g). For a fjord width of 2 km, plume and return flow float velocities are largest slightly above the fjord centerline and decrease toward the fjord walls due to boundary effects (Figures 7a and 7b). As the fjord width is increased to 5 km, the near-glacier plume forms a narrow jet that tends toward the north wall, generating a pair of small cyclonic and anticyclonic recirculation cells to the south and north of the vertical plume, respectively (Figure 7c). As the plume evolves down-fjord, the largest along-fjord velocities are found near the north wall. Return flow floats are advected toward the southeast over the sill, with maximum float densities concentrated slightly below the fjord centerline in the slow return flow (Figure 7d). For fjord widths of 10 and 20 km, the near-glacier jet transitions into a boundary current over a ∼10 and ∼20 km horizontal length scale, respectively (Figures 7e and 7g). As the boundary current flows down-fjord along the north wall it then veers southward, generating a large geostrophically-balanced cyclonic recirculation cell (supporting information Text S1 and Figure S4). Plume float densities are largest in the north stagnation cell above the vertical plume, the near-terminus region behind the float release location, and in the shear magins of the plume where vorticity is elevated. For these wide fjords, the return flow toward the glacier forms a slow, narrow boundary current that is constrained to the south wall (Figures 7f and 7h).

Plume float residence time (the time required for the float to transit the length of the fjord) generally increases with fjord width, with distributions exhibiting higher positive skew in wide fjords (Figure 8a). Median plume float residence times are 6.79, 14.7, 24.2, and 18.3 days for corresponding fjord widths of 2, 5, 10, and 20 km, respectively. Plume floats are freshened and cooled as the fjord widens, due to increased recirculation-driven mixing of ambient waters into the outflowing plume. For the narrowest fjord examined ($W = 2$ km), plume float cross-fjord position is fairly uniform across the width of the fjord, with a median value of ∼0.61 (cross-fjord position of 1 is at the north wall). As the fjord width is increased to 5 km, the median cross-fjord position shifts to ∼0.73, with plume float position biased toward the north wall. For larger fjord widths ($W = 10$ and 20 km), cross-fjord position distributions become bimodal, as the plume bifurcates into a outflow on the northern wall and recirculation cells that span the fjord width. For the widest fjord simulated ($W = 20$ km), recirculation dominates the distribution, shifting the median cross-fjord position southward to ∼0.40. Residence time for return flow floats also increase with fjord width (Figure 8b), with median plume float residence times of 32.7, 42.6, 42.8, and 49.7 days for fjord widths of 2, 5, 10,

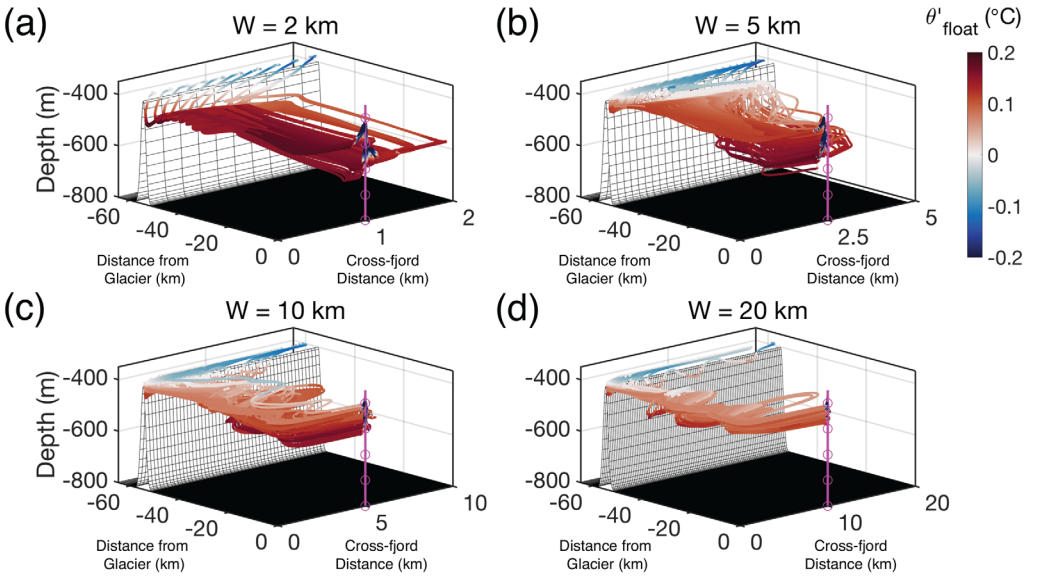

Figure 9. Return flow float trajectory and potential temperature anomaly for varying fjord width. Sill-glacier geometry corresponds to $H_s/H = 0.5$, $H_{gf}/H = 1$; subglacial discharge flux is 250 $m^3\ s^{-1}$. Return flow floats spanning the width of the fjord are time-released daily after day 30 near the fjord mouth slightly below sill depth (x = −58 km; z = −390 m). The final 200 floats to successfully transit from the fjord mouth to the first wet cell adjacent to the glacier (x = −200 m) are shown. Vertical magenta line represents the vertical plume centerline; circles show 100 m depth intervals. Potential temperature anomaly is taken with respect to the initial model conditions at the float depth.

and 20 km, respectively. Return flow floats become warmer and saltier (less diluted) as the fjord widens, with reduced spread in potential temperature and salinity distributions. For the widest fjord simulated ($W = 20$ km), return flow float cross-fjord position converges to a narrow distribution slightly above the south wall of the fjord, with a median value of ∼0.15.

Examination of return flow float trajectories demonstrates that rapid drawdown of basin waters by the vertical plume in narrow fjords allows for the return flow to cascade deep into the fjord basin. (Figure 9a). For the initial fjord hydrography used in this study (i.e., ambient conditions), potential temperature below the near-surface layer reaches a maximum slightly above the sill and progressively cools at depth (e.g., Figure 1c). This temperature stratification results in return flow floats that exhibit negative potential temperature anomalies as they are advected over the sill and shoal. Potential temperature anomalies then become increasingly positive as the return flow floats cascade into the cooler basin; this effect is most pronounced in narrow fjords. As the fjord widens, the vertical plume becomes less efficient at drawing down basin waters, resulting in a shallower return flow of sill depth water toward the glacier (Figures 9b and 9c). For the widest fjord simulated, the return flow is located along the south wall slightly below sill depth (Figure 9d). Maximum depths reached by the return flow floats are 663, 590, 521, and 490 m for corresponding fjord widths of 2, 5, 10, and 20 km, respectively.

3.2. Tidal Forcing

To investigate how tidal forcing modulates the inflow of deep shelf waters in narrow and wide fjords, we first focus on simulations with a shallow sill ($H_s/H = 0.25$) and tidal forcing only (i.e., no subglacial discharge; Table 1, green cells). For all tidal simulations, baroclinic tidal velocities over the sill are less than the mode-1 internal wave phase speed, implying a subcritical flow regime (i.e., Froude number < 1). For a fjord width of 2 km, the interaction of the barotropic tide with a shallow sill generates internal tides that reflect off the glacier wall, leading to a two-dimensional partially-standing wave response in the fjord and resulting in an intrusion of DST that extends to within ∼20 km of the glacier (Figure 10a). As the fjord width is increased to 10 km, the internal tide propagates cyclonically around the fjord basin as an internal Kelvin wave, producing an intrusion of DST that spans the horizontal extent of the fjord and reaches the glacier face. (Figure 10b and supporting information Movies S1 and S2). For both fjord widths, maximum DST concentrations are located slightly below sill depth, with concentrations of 0.5 confined to depths between 100 and 300 m. For a fjord width of 2 km, DST concentrations of 0.5 intrude ∼21 km into the fjord basin and exhibit a diffuse frontal structure (Figure 10a). Using the maximum tidal velocity observed over the sill (0.39 m s^{-1}) yields a

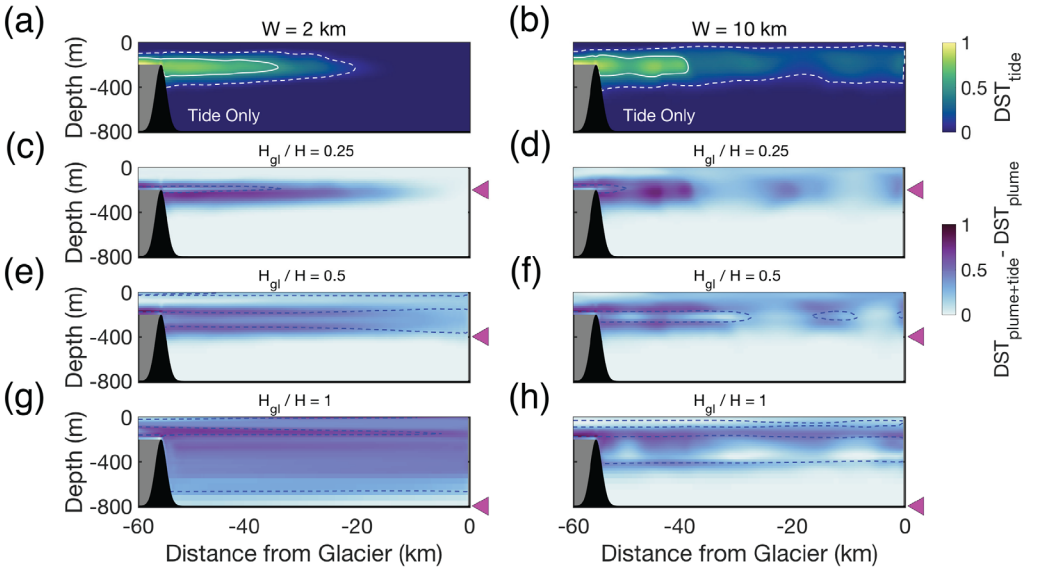

Figure 10. Along-fjord DST concentration for varying fjord-glacier geometry and forcing. Sill geometry corresponds to $H_s/H = 0.25$; subglacial discharge flux is 250 $m^3\ s^{-1}$. Shaded colors in Figures 10a and 10b represent DST concentration for simulations with tidal forcing only (DST_{tide}); dashed and solid white contours show tracer concentration of 0.1 and 0.5, respectively. Shaded colors in Figure 10c through Figure 10h show the difference in DST concentration between vertical plume + tidal forcing and vertical plume only simulations ($DST_{plume+tide}$ - DST_{plume}). Dashed blue contours show tracer concentration of 0.1 for the vertical plume only case; gray colors show region where DST tracer is restored. Simulations with tidal forcing are filtered with a Godin filter. DST concentrations are averaged in the cross-fjord direction and over day 84–114 (to account for filter window edge effects); left-pointing triangles in Figure 10c through Figure 10h represent grounding line depth.

tidal excursion of ~8.7 km. As the fjord width increases to 10 km, the front sharpens and the modeled intrusion reaches a smaller distance of only ~16 km (Figure 10b). In this wider fjord, maximum tidal velocities at the sill increase to 0.57 m s^{-1}, with a corresponding tidal excursion of ~12.5 km.

Simulations with both vertical plume and tidal forcing reveal how tide-sill interactions modify the vertical structure of DST in the basin (Figures 10c–10h). For systems grounded above sill depth ($H_{gl}/H = 0.25$), the addition of tidal forcing primarily increases DST concentrations directly below the sill depth, with equivalent intrusion lengths compared to the simulations with tidal forcing alone (Figures 10c and 10d). For glaciers grounded below sill depth ($H_{gl}/H = 0.5$), the largest increase in DST concentration occurs directly above the sill and at the maximum depth of the internal wave vertical excursion (~280 m) (Figures 10e and 10f). For a deep glacier in a 2 km wide fjord ($H_{gl}/H = 1$), DST concentrations increase most substantially in a thin layer above the sill depth (Figure 10g). In the 10 km wide fjord, the increase in DST from tide-sill interactions exhibits patchier structure and is primarily confined to the upper 400 m (Figure 10h). For all fjord widths examined, the addition of tidal forcing has a limited impact on the export of basin water (<10% decrease in fjord basin fraction at day 120); however, the composition of basin waters is substantially modified by tides (supporting information Figure S5). Simulations with tidal forcing only in 2 and 10 km wide fjords result in DST fractions of 0.09 and 0.14 at day 120, respectively. Combining vertical plume forcing and tides in a 2 km (10 km) wide fjord increases DST fraction at day 120 compared to the tidal forcing only case by ~1476 (5060), 160 (410), and 126 (141)% for a corresponding H_{gl}/H of 0.25, 5, and 1. We note that including ambient melt in the tidal simulations has a negligible effect on DST fractions (<1% change).

3.3. Wind Forcing

We next consider the influence of along-fjord and along-shelf wind stress on fjord circulation (Figure 11; Table 1, red cells). For a 2 km wide fjord, 3 day along-fjord wind forcing (black line) drives a strong outflow in the upper 40 m, resulting in a maximum out-fjord volume transport of −32.87 mSv during peak wind stress at day 121.5 (Figure 11a). During the wind event, isopycnals in the upper 50 m of the water column at the sill crest are heaved ~50 m in the vertical and outcrop (not shown). The wind-driven flow is primarily baroclinic, with a small net inflow of ~30 $m^3\ s^{-1}$ during peak wind forcing. As wind stress is reduced, out-fjord volume transport decreases to −7.23 mSv (day 123.25). During relaxation, flow in the upper layer

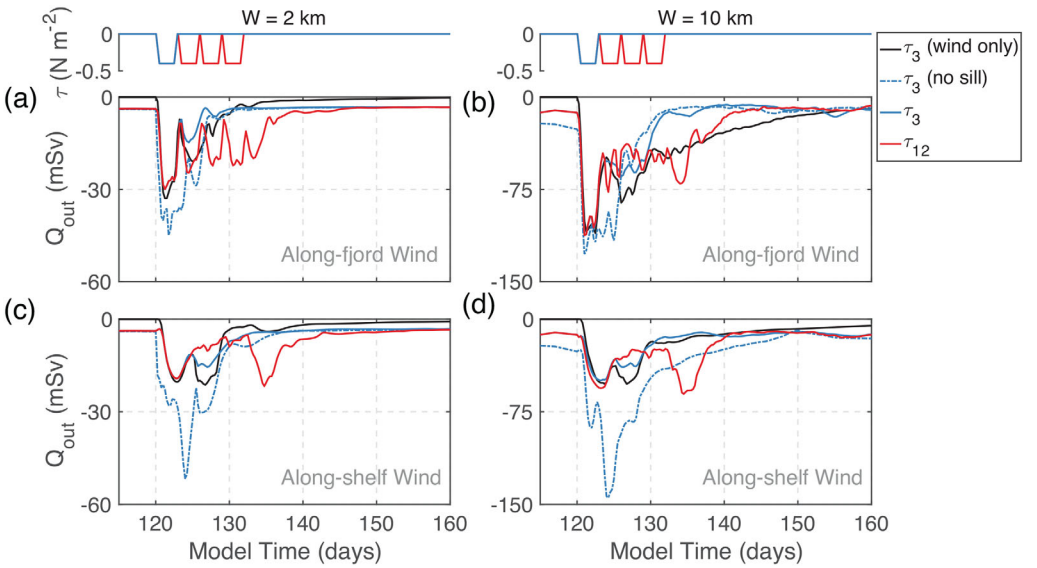

Figure 11. Time-varying out-fjord volume transport computed at the sill crest for varying fjord geometry and wind forcing. (a and b) Along-fjord wind forcing in a 2 and 10 km wide fjord; (c and d) The corresponding along-shelf wind forcing case. Sill-glacier geometry corresponds to $H_s/H = 0.25$, $H_g/H = 0.25$; subglacial discharge flux is 250 $m^3\ s^{-1}$. Solid black lines show simulations with wind stress forcing only. Solid blue and red lines show vertical plume and 3 and 12 day wind forcing, respectively. Dashed blue lines show vertical plume and 3 day wind forcing with no sill. Note the different scales used on the *y* axis and that the wind forcing (red and blue curves) shown in the top row overlaps over day 120–123.

reverses direction toward the glacier (supporting information Figure S6), with a compensating out-fjord transport in the lower layer of −20.87 mSv (day 125). Several small oscillations occur during spin-down, with out-fjord volume transport diminishing to −0.25 mSv by day 160. For the 10 km wide fjord, maximum volume transports are increased by roughly a factor of 4 (Figure 11b). In this wide fjord, along-fjord winds produce an Ekman transport-driven convergence along the north wall, depressing isopycnals and resulting in a geostrophic flow that persists during spin-down (not shown). Along-shelf winds in a 2 km wide fjord result in a smaller peak out-fjord volume transport of −21.27 mSv, increasing to −52.49 mSv for a 10 km wide fjord (Figures 11c and 11d). We note that along-shelf winds have a limited influence on cross-fjord density structure, reducing the timescale for spin-down compared to the along-fjord wind case shown in Figure 11b.

Simulations with both vertical plume and wind forcing (blue and red lines) show that wind-driven circulation dominates over the buoyancy-driven exchange flow. For a fjord width of 2 (10) km, 3 day along-fjord winds amplify the exchange flow by a factor of ∼7.5 (8.6). Maximum volume transports are comparable to simulations with wind forcing only (Figures 11a and 11b); transports in simulations with mid-depth and deep grounding lines also converge to wind only values (not shown). For 3 day along-shelf winds, the exchange flow in the 2 km (10 km) wide fjord is amplified by a factor of ∼5.2 (2.3) (Figures 11c and 11d). For all fjord widths examined, exclusion of the shallow sill (i.e., no sill; dashed blue line) elevates volume transport; the largest increases are observed in the along-shelf wind simulations. For 12 day along-fjord winds (red line), volume transports reach maximum values during the first "top hat" forcing event (Figure 11a,b). In contrast, 12 day along-shelf wind simulations have comparable volume transports during peak wind forcing and relaxation (day 134) (Figures 11c and 11d). Integrating out-fjord volume transports over the 12 day along-fjord wind forcing period in the 10 km wide fjord (Figure 11b) yields a cumulative transport of -6.14×10^{10} m^3, approximately 14% of the basin volume. For equivalent fjord-glacier geometry, the vertical plume forcing only case results in a 12 day cumulative out-fjord transport (computed from model day 108 to 120) of -1.62×10^{10} m^3, roughly 4% of the basin volume.

4. Discussion

4.1. Overview

In contrast to typical fjord systems, tidewater glacier fjords can have substantial fluxes of meltwater and subglacial runoff at depth; this subsurface buoyancy forcing provides a mechanism for renewal that is

independent of external shelf forcing. Our results demonstrate that, for these systems, fjord-glacier geometry is a first order control on subglacial discharge-driven circulation and renewal of basin waters. While our simulations are idealized and focus on steady buoyancy forcing from subglacial discharge, we have several key results: 1) glaciers grounded below sill depth can renew basin waters with subglacial discharge plumes, 2) rotational effects in wide fjords generate vigorous recirculation and dilution in the outflowing plume and constrains the return flow to a narrow boundary current along the south wall, and 3) tidal mixing over the sill increases plume-driven transport of deep shelf waters into the basin. We stress that varying the geometric parameters examined in this study (fjord width, sill depth, and grounding line depth) can produce marked differences in fjord circulation and hydrography, which may contribute to significant contrasts among adjacent fjord/glacier systems [*Bartholomaus et al*., 2016]. As new bathymetric and glacier bed elevation surveys become available in the future [*Morlighem et al*., 2016], we expect these results to guide future estuarine box model parameterizations [*Garvine and Whitney*, 2006; *Gillibrand et al*., 2013; *Tseng et al*., 2016] of tidewater glacier fjords in large-scale climate models.

4.2. Renewal of Basin Waters

Previous work in Fennoscandia and Greenland fjords has focused on renewal of basin waters below the sill depth driven primarily by fjord-shelf density gradients [*Aure and Stigebrandt*, 1990; *Aure et al*., 1996; *Mortensen et al*., 2011, 2013, 2014; *Jackson et al*., 2014] and diapycnal mixing [*Stigebrandt and Aure*, 1989]. Our simulations demonstrate that subglacial discharge emerging from glaciers grounded below the sill depth can be an efficient, seasonal mechanism for renewal (Figure 6). These results are consistent with previous two-dimensional modeling efforts that suggest subglacial discharge from Jakobshavn Glacier can drive substantial renewal of the fjord basin over a summer season [*Gladish et al*., 2015]. We note that depending on the sill depth and terminal level of the plume, subglacial discharge-driven renewal of basin waters may transition between distinct seasonal modes. During winter, and or, during the onset/end of the meltwater season when discharge is weak, fjord basins with shallow sills may act as a weakly-ventilated or closed control volumes. In this mode, the basin may act as a "filling box" [*Baines and Turner*, 1969], where the outflowing plume is blocked by the sill and progressively fills the basin downward from the initial level of neutral buoyancy (Figure 4a). For this closed system, glacially-modified waters from the plume will, at some later time, be reentrained in the vertical plume at the terminus [*Killworth and Turner*, 1982], which may cool vertical plume waters and decrease melt rates. As discharge increases during the meltwater season, the plume's terminal level may shoal above sill depth, transitioning the basin to an open control volume and allowing for plume-driven exchange with the shelf (Figures 4b–4d). We acknowledge that our choice of steady subglacial discharge from a single point source vertical plume is highly idealized; we would expect significant temporal variability in the subglacial hydrologic network over the duration of the meltwater season [*Slater et al*., 2017]. For equivalent subglacial discharge, an increase in the number of subglacial conduits or use of line plume geometry would decrease the terminal level of the plume and amplify the strength of the exchange flow [*Carroll et al*., 2015; *Cowton et al*., 2015].Additionally interactions between the plume, subsurface buoyancy fluxes from iceberg melt [*Sulak*, 2016; *Enderlin et al*., 2016], and episodic shelf-driven dense inflows [*Mortensen et al*., 2011, 2013, 2014] may significantly modulate these renewal processes; assessment of potential feedbacks between these mechanism requires additional simulations beyond the scope of this paper.

4.3. Rotational Effects

Our simulations also suggest that the outflowing plume may be susceptible to instability as it flows downfjord, resulting in larger volume transports and dilution than predicted by the buoyant plume theory [*Cowton et al*., 2015; *Slater et al*., 2016] used in our vertical plume parameterization. In the near-glacier field, the outflowing plume develops into a anticyclonic vortex, with cyclonic rotation in the deep return flow (Figures 2 and 3), similar to previous theoretical [*Speer*, 1989; *Speer and Marshall*, 1995a], laboratory [*Fernando et al*., 1998], and numerical modeling studies [*Deremble*, 2016] of convective point source plumes in rotating systems. For the shallow grounding line case, the surface-confined plume exhibits instability in both the near-glacier region and along the north wall of the fjord (Figures 2b–2d). The shedding of anticyclonic vortices in the near-glacier plume and development of finite amplitude waves in the outflowing boundary current is consistent with previous studies of baroclinic instability in rotating, convective plumes [*Helfrich and Battisti*, 1991; *Speer and Marshall*, 1995b] and buoyancy-driven costal density currents [*Qiu et al*., 1988]. Diagnosing the Ertel potential vorticity reveals that the cross-fjord potential vorticity changes sign in both the near-

glacier region and along the north wall (not shown), a necessary condition for baroclinic instability [*Pedlosky*, 1987; *Pickart et al*., 2005]. We note that the instability present in our simulations is sensitive to the choice of eddy viscosity; increasing the horizontal eddy viscosity by an order of magnitude suppresses instability in the plume. These results, along with recent work detailing instability in meltwater outflows from Antarctic ice shelves [*Garabato et al*., 2017], motivate the need for further high-resolution modeling studies of subglacial plumes in rapidly rotating systems.

Additionally, this work shows that rotational effects are an important control on the lateral structure of the exchange flow in wide, high-latitude fjords. For a fjord width of 10 km (slightly below twice the internal deformation radius computed from initial model hydrography), the plume develops geostrophically-balanced recirculation cells downstream of the glacier (Figure 7 and supporting information Figure S4), increasing entrainment of ambient waters in the plume and significantly diluting the outflow of glacially-modified waters (Figures 5b and 5c). Observations of iceberg trajectories from west and southeast Greenland [*Sutherland et al*., 2014a; *Sulak et al*., 2017] support these modeling results, showing significant recirculation and cross-fjord velocity gradients in the wider regions of the fjord. Additionally, the smaller stagnation cells to the north of the vertical plume (Figures 7c and 7e) suggest that plume waters may be distributed unevenly along glacier termini. Our simulations also demonstrate that rotational effects can significantly constrain the cross-fjord structure of shelf waters intruding into the fjord. For wide fjords, the return flow consists of a slow, narrow boundary current that flows along the south wall (Figures 7f and 7h). These results imply that wide fjords may exhibit significant cross-fjord gradients in heat transport, which could contribute to spatial heterogeneity in submarine melt rates along the terminus. We anticipate that slow, rotationally-influenced outflows driven by ambient terminus melt may form similar boundary currents along the north wall. Recent observations from Petermann Glacier in northwest Greenland support this hypothesis, showing that meltwater is exported in a boundary current that is constrained along the northeast side of the fjord [*Heuzé et al*., 2016]. We note that our simulations do not explore variations in fjord length; however, we anticipate our results to hold over a range of along-fjord length scales, as long as the mouth region lies outside of any recirculation cells.

4.4. External Forcing

For our choice of peak wind stress magnitude, we find that synoptic wind significantly amplifies the subglacial discharge-driven exchange flow. *Moffat* [2014] also shows that along-fjord wind forcing can be an important mechanism for modulating buoyancy-driven circulation in tidewater glacier fjords, with in-fjord transport increasing by a factor of 2.5 for a wind stress magnitude of $\sim$0.1 N m^{-2}. Our simulations are in general agreement with these results; the subglacial discharge-driven exchange flow can be increased by roughly a factor of 8 for our maximum along-fjord wind stress of -0.4 N m^{-2}. While wind stress may be an important mechanism for amplifying the exchange flow, strong near-surface stratification limits wind-induced vertical mixing to the upper water column (supporting information Text S2 and Figure S7). In contrast, tides result in significant mixing of basin waters above the sill depth and increase the inflow of deep shelf waters in the basin. Observations from Godthåbsfjord in west Greenland also highlight the importance of tidal mixing in shallow-silled tidewater glacier fjords [*Mortensen et al*., 2011]. In Godthåbsfjord, tidal mixing of warm, fresh near-surface waters over the sill drives a baroclinic circulation in the fjord, providing an important source of local heat for submarine melt during summer and early winter. We note that our vertical plume parameterization does not provide an adequate buoyancy flux to restratify tidally-mixed waters, stressing the need for parameterizations of subsurface iceberg melt [*Enderlin et al*., 2016] in future modeling efforts. Additionally, we acknowledge that our simulations use initial model hydrography from a single fjord; the use of stratification profiles from a variety of fjords may modulate the vertical extent of wind and tidal mixing.

Our simulations, in agreement with previous models of Arctic fjords [*Støylen and Fer*, 2014], also demonstrate that tide-sill interactions in wide fjords can generate internal Kelvin waves. Propagating internal Kelvin waves can result in a wave-induced mass flux [*Støylen and Weber*, 2010], which could be responsible for the elevated transport of deep shelf waters in our tidal simulations with wide fjords (supporting information Figure S5b). It should be noted that for our choice of baroclinic tidal velocities ($<$0.6 m s^{-1}), the flow regime at the sill is subcritical, limiting our parameter space to "wave type" fjords [*Stigebrandt and Aure*, 1989]. For model simulations with larger tidal amplitudes or severely-constricted sills, fjord-shelf exchange may be determined by hydraulic control [*Farmer and Freeland*, 1983; *Farmer and Denton*, 1985]. Additionally, we

Table 2. Geometric Parameters for Various Tidewater Glacier Fjords

Tidewater Glacier Name	Location	W^a (km)	H^b (m)	H_s/H^c	H_{gl}/H^d	H_{gl}/H_s	Reference
LeConte	SE Alaska	1–2	350	0.06	0.71	12.5	*Motyka et al.* [2003, 2013]
Columbia	SE Alaska	2–5	480	0.04	0.88	21.0	*Love et al.* [2016]
Jorge Montt	Patagonia	1.8–5	380	0.12	0.74	6.22	*Moffat* [2014]
Kangerdlugssuaq	SE Greenland	5–20	900	0.5	0.72	1.44	*Cowton et al.* [2016]
Helheim	SE Greenland	5–13	650	0.85	1	1.18	*Sutherland et al.* [2014b]
Kangiata Nunata Sermia	W Greenland	4.5–6.5	620	0.27	0.40	1.47	*Mortensen et al.* [2011, 2013, 2014]
Jakobshavn	W Greenland	4.5–9	800	0.25	1	4.00	*Gladish et al.* [2015]
Store	W Greenland	6–7	800	1	0.63	1.60	*Rignot et al.* [2016]
Rink Isbrae	NW Greenland	5–15	1100	0.39	0.77	1.98	*Bartholomaus et al.* [2016]
Kangerlussuup Sermia	NW Greenland	4–6	550	0.75	0.45	0.61	*Bartholomaus et al.* [2016]

[a]Minimum and maximum width of fjord.
[b]Maximum depth of fjord.
[c]Computed using depth of the shallowest sill in the fjord.
[d]Computed using mean grounding line depth.

have neglected spring-neap variability in our idealized tidal forcing, which could lead to supercritical conditions during spring tides and the development of tidal jets [*Stashchuk et al.*, 2007]. For the grid size aspect ratio used in this study ($\Delta z/\Delta x$ of 0.1 at sill crest) a hydrostatic model is justified as nonhydrostatic pressure effects are small [*Berntsen et al.*, 2009]. However, we acknowledge that hydraulics and exchange processes at the sill are not explicitly resolved in our simulations.

4.5. Implications for High-latitude Fjords

This work demonstrates that the depth of the grounding line compared to the sill (i.e., H_{gl}/H_s) is a key control on subglacial discharge-driven renewal, suggesting that this parameter could be used *a priori* to identify fjords where basin renewal may occur independently of external shelf forcing. A comparison of various high-latitude tidewater glacier fjords (Table 2) reveals significant heterogeneity in the geometric parameters examined in this study. Tidewater glacier fjords with shallow sills and grounding lines (e.g., LeConte and Jorge Montt) may act more like typical fjord systems, with a near-surface exchange flow and deep renewal primarily driven by shelf processes or wind stress [*Moffat*, 2014]. For the deeper grounding line in Columbia Glacier fjord, a subsurface plume would be trapped below the shallow sill, which could fill the basin with cold subglacial discharge [*Walters et al.*, 1988]. In deeply-grounded systems without significant sills (e.g., Helheim and Kangerdlugssuaq), we would expect subglacial discharge-driven renewal to be active and rotationally controlled in the wider regions of the fjord; however, this process may be masked by strong shelf-driven intermediary flows [*Straneo et al.*, 2010; *Sutherland and Straneo*, 2012; *Jackson et al.*, 2014]. For deeply-grounded systems in west Greenland where shelf winds are weaker (e.g., Jakobshavn and Rink fjord), we might expect subglacial discharge to be the dominant mechanism for renewal during the meltwater season; systems that are grounded above, or near, the sill depth (e.g., Kangerlussuup Sermia) would rely more on dense coastal inflows for renewal [*Mortensen et al.*, 2011]. We note that glacier retreat along a retrograde bed would deepen the grounding line, which could increase cumulative entrainment into the vertical plume and result in a stronger depth-integrated exchange (Figure 5). This process may increase ocean heat transport toward the glacier and provide an additional positive feedback to the tidewater glacier cycle. Retreat along seaward-sloping beds could shoal the return flow above sill depth (i.e., $H_{gl}/H_s < 1$), limiting subglacial discharge-driven renewal of basin waters. Ultimately, coupled ocean-glacier models are needed to quantify potential feedbacks between the vertical plume/exchange flow and glacier dynamics.

5. Summary and Conclusions

Tidewater glacier fjords complicate the classic model of fjord circulation and renewal, due to subsurface buoyancy forcing from submarine melt and subglacial discharge. These systems provide a critical pathway for the export of glacially-modified waters to the coastal ocean and flow of warm ocean waters toward the ice. However, we still lack a precise understanding of how circulation in tidewater glacier fjords is modulated by fjord-glacier geometry. Here we use a suite of high-resolution ocean simulations to investigate how the subglacial plume-driven exchange flow depends on fjord-glacier geometry and external forcing from tides and wind stress. We have several critical results:

1. Glaciers grounded below sill depth can draw shelf waters over a shallow sill and into fjord basins with seasonal subglacial discharge; this process is independent of external shelf forcing.
2. Rotational effects strongly control the cross-fjord structure of the exchange flow in wide fjords; in these systems, plumes develop geostrophically-balanced recirculation cells that increase the dilution and residence time of glacially-modified waters.
3. In narrow fjords the rapid drawdown of basin waters by the vertical plume allows shelf waters to cascade deep into the basin; in wide fjords the return flow consists of a thin, boundary current that flows toward the terminus slightly below sill depth.
4. Wind stress can significantly amplify the subglacial discharge-driven exchange flow; however, strong near-surface stratification limits wind-induced mixing to the upper water column.
5. Tidal mixing over a sill increases in-fjord transport of deep shelf waters and erodes ambient stratification in the basin.

Our simulations provide key insight for the development of estuarine box model parameterizations of tidewater glacier fjords and stress the need to include sea ice and iceberg melt in future fjord-scale modeling efforts that include external forcing. Ultimately, improved estimates of fjord-glacier bed topography, along with sustained observations of deep basin waters, are critical for understanding spatiotemporal variability in submarine melt rates across Greenland.

Acknowledgments
This work was partially supported by the National Aeronautics and Space Administration grant NNX12AP50G, National Science Foundation Division of Polar Programs grant 1504521, and the University of Oregon. Data and model simulations used in this work are available from the authors upon request (dcarroll@uoregon.edu). We would like to thank the thoughtful and constructive criticism of this work provided by two anonymous reviewers.

References

Adcroft, A., C. Hill, and J. Marshall (1997), Representation of topography by shaved cells in a height coordinate ocean model, *Mon. Weather Rev.*, *125*(9), 2293–2315.

Arakawa, A., and V. R. Lamb (1977), Computational design of the basic dynamical processes of the UCLA general circulation model, *Methods Comput. Phys.*, *17*, 173–265.

Arneborg, L., and B. Liljebladh (2009), Overturning and dissipation caused by baroclinic tidal flow near the sill of a fjord basin, *J. Phys. Oceanogr.*, *39*(9), 2156–2174.

Arneborg, L., C. P. Erlandsson, B. Liljebladh, and A. Stigebrandt (2004), The rate of inflow and mixing during deep-water renewal in a sill fjord, *Limnol. Oceanogr. Methods*, *49*(3), 768–777.

Aure, J., and A. Stigebrandt (1990), Quantitative estimates of the eutrophication effects of fish farming on fjords, *Aquaculture*, *90*(2), 135–156.

Aure, J., J. Molvær, and A. Stigebrandt (1996), Observations of inshore water exchange forced by a fluctuating offshore density field, *Mar. Pollut. Bull.*, *33*(1), 112–119.

Baines, W., and J. Turner (1969), Turbulent buoyant convection from a source in a confined region, *J. Fluid Mech.*, *37*(1), 51–80.

Bamber, J., M. van den Broeke, J. Ettema, J. Lenaerts, and E. Rignot (2012), Recent large increases in freshwater fluxes from Greenland into the North Atlantic, *Geophys. Res. Lett.*, *39*, L19501, doi:10.1029/2012GL052552.

Bartholomaus, T. C., et al. (2016), Contrasts in the response of adjacent fjords and glaciers to ice-sheet surface melt in west Greenland, *Ann. Glaciol.*, *57*(73), 1–14.

Beaird, N., F. Straneo, and W. Jenkins (2015), Spreading of Greenland meltwaters in the ocean revealed by noble gases, *Geophys. Res. Lett.*, *42*, 7705–7713, doi:10.1002/2015GL065003.

Bendtsen, J., J. Mortensen, and S. Rysgaard (2015), Modelling subglacial discharge and its influence on ocean heat transport in arctic fjords, *Ocean Dyn.*, *65*(11), 1535–1546.

Berntsen, J., J. Xing, and A. M. Davies (2009), Numerical studies of flow over a sill: Sensitivity of the non-hydrostatic effects to the grid size, *Ocean Dyn.*, *59*(6), 1043–1059.

Carroll, D., D. A. Sutherland, E. L. Shroyer, J. D. Nash, G. A. Catania, and L. A. Stearns (2015), Modeling turbulent subglacial meltwater plumes: Implications for fjord-scale buoyancy-driven circulation, *J. Phys. Oceanogr.*, *45*(8), 2169–2185.

Carroll, D., et al. (2016), The impact of glacier geometry on meltwater plume structure and submarine melt in Greenland fjords, *Geophys. Res. Lett.*, *43*, 9739–9748, doi:10.1002/2016GL070170.

Chauché, N., A. Hubbard, J.-C. Gascard, J. Box, R. Bates, M. Koppes, A. Sole, P. Christoffersen, and H. Patton (2014), Ice–ocean interaction and calving front morphology at two west Greenland tidewater outlet glaciers, *Cryosphere*, *8*(4), 1457–1468.

Cottier, F., V. Tverberg, M. Inall, H. Svendsen, F. Nilsen, and C. Griffiths (2005), Water mass modification in an arctic fjord through cross-shelf exchange: The seasonal hydrography of Kongsfjorden, Svalbard, *J. Geophys. Res.*, *110*, C12005, doi:10.1029/2004JC002757.

Cowton, T., D. Slater, A. Sole, D. Goldberg, and P. Nienow (2015), Modeling the impact of glacial runoff on fjord circulation and submarine melt rate using a new subgrid-scale parameterization for glacial plumes, *J. Geophys. Res. Oceans*, *120*, 796–812, doi:10.1002/2014JC010324.

Cowton, T., A. Sole, P. Nienow, D. Slater, D. Wilton, and E. Hanna (2016), Controls on the transport of oceanic heat to Kangerdlugssuaq glacier, east Greenland, *J. Glaciol.*, *62*(236), 1167–1180.

Deremble, B. (2016), Convective plumes in rotating systems, *J. Fluid Mech.*, *799*, 27–55.

Enderlin, E. M., I. M. Howat, S. Jeong, M.-J. Noh, J. H. Angelen, and M. R. Broeke (2014), An improved mass budget for the Greenland ice sheet, *Geophys. Res. Lett.*, *41*, 866–872, doi:10.1002/2013GL059010.

Enderlin, E. M., G. S. Hamilton, F. Straneo, and D. A. Sutherland (2016), Iceberg meltwater fluxes dominate the freshwater budget in Greenland's iceberg-congested glacial fjords, *Geophys. Res. Lett.*, *43*, 11,287–11,294, doi:10.1002/2016GL070718.

Farmer, D. M., and R. A. Denton (1985), Hydraulic control of flow over the sill in observatory inlet, *J. Geophys. Res.*, *90*(C5), 9051–9068.

Farmer, D. M., and H. J. Freeland (1983), The physical oceanography of fjords, *Prog. Oceanogr.*, *12*(2), 147–220.

Fernando, H., R. Chen, and B. Ayotte (1998), Development of a point plume in the presence of background rotation, *Phys. Fluids*, *10*(9), 2369–2383.

Garabato, A. C. N., A. Forryan, P. Dutrieux, L. Brannigan, L. C. Biddle, K. J. Heywood, A. Jenkins, Y. L. Firing, and S. Kimura (2017), Vigorous lateral export of the meltwater outflow from beneath an Antarctic ice shelf, *Nature*, *542*(7640), 219–222.
Garvine, R. W., and M. M. Whitney (2006), An estuarine box model of freshwater delivery to the coastal ocean for use in climate models, *J. Mar. Res.*, *64*(2), 173–194.
Geyer, W., and G. Cannon (1982), Sill processes related to deep water renewal in a fjord, *J. Geophys. Res.*, *87*(C10), 7985–7996.
Geyer, W., and D. Ralston (2011), The dynamics of strongly stratified estuaries, in *Treatise on Estuarine and Coastal Science*, vol. 2, edited by E. Wolanski and D. Mclusky, pp. 37–51, Academic Press, Elsevier, Waltham.
Gillibrand, P. A., M. E. Inall, E. Portilla, and P. Tett (2013), A box model of the seasonal exchange and mixing in regions of restricted exchange: Application to two contrasting Scottish inlets, *Environ. Modell. Software*, *43*, 144–159.
Gladish, C. V., D. M. Holland, A. Rosing-Asvid, J. W. Behrens, and J. Boje (2015), Oceanic boundary conditions for jakobshavn glacier: part i: Variability and renewal of ilulissat icefjord waters, 2001–14*, *J. Phys. Oceanogr.*, *45*(1), 3–32.
Godin, G. (1991), The analysis of tides and currents, in *Tidal Hydrodynamics*, edited by B. B. Parker, pp. 675–709, John Wiley, New York.
Harden, B., I. Renfrew, and G. Petersen (2011), A climatology of wintertime barrier winds off southeast Greenland, *J. Clim.*, *24*(17), 4701–4717.
Helfrich, K. R., and T. M. Battisti (1991), Experiments on baroclinic vortex shedding from hydrothermal plumes, *J. Geophys. Res.*, *96*(C7), 12,511–12,518.
Heuzé, C., A. Wåhlin, H. L. Johnson, and A. Münchow (2016), Pathways of meltwater export from Petermann glacier, Greenland, *J. Phys. Oceanogr.*, *47*(2), 405–418.
Holland, D., and A. Jenkins (1999), Modeling thermodynamic ice-ocean interactions at the base of an ice shelf, *J. Phys. Oceanogr.*, *29*(8), 1787–1800.
Huang, R. X. (1993), Real freshwater flux as a natural boundary condition for the salinity balance and thermohaline circulation forced by evaporation and precipitation, *J. Phys. Oceanogr.*, *23*(11), 2428–2446.
Inall, M., F. Cottier, C. Griffiths, and T. Rippeth (2004), Sill dynamics and energy transformation in a jet fjord, *Ocean Dyn.*, *54*(3–4), 307–314.
Jackett, D. R., and T. J. Mcdougall (1995), Minimal adjustment of hydrographic profiles to achieve static stability, *J. Atmos. Oceanic Technol.*, *12*(2), 381–389.
Jackson, R., and F. Straneo (2016), Heat, salt, and freshwater budgets for a glacial fjord in Greenland, *J. Phys. Oceanogr.*, *46*(9), 2735–2768.
Jackson, R., F. Straneo, and D. Sutherland (2014), Externally forced fluctuations in ocean temperature at Greenland glaciers in non-summer months, *Nat. Geosci.*, *7*(7), 503–508.
Jenkins, A. (2011), Convection-driven melting near the grounding lines of ice shelves and tidewater glaciers, *J. Phys. Oceanogr.*, *41*(12), 2279–2294.
Killworth, P., and J. Turner (1982), Plumes with time-varying buoyancy in a confined region, *Geophys. Astrophys. Fluid Dyn.*, *20*(3–4), 265–291.
Klinck, J. M., J. J. O'Brien, and H. Svendsen (1981), A simple model of fjord and coastal circulation interaction, *J. Phys. Oceanogr.*, *11*(12), 1612–1626.
Large, W. G., J. C. McWilliams, and S. C. Doney (1994), Oceanic vertical mixing: A review and a model with a nonlocal boundary layer parameterization, *Rev. Geophys.*, *32*(4), 363–403.
Love, K. B., B. Hallet, T. L. Pratt, and S. O'Neel (2016), Observations and modeling of fjord sedimentation during the 30 year retreat of Columbia glacier, AK, *J. Glaciol.*, *62*(234), 778–793.
Mankoff, K. D., F. Straneo, C. Cenedese, S. B. Das, C. G. Richards, and H. Singh (2016), Structure and dynamics of a subglacial discharge plume in a Greenlandic fjord, *J. Geophys. Res. Oceans*, *121*, 8670–8688, doi:10.1002/2016JC011764.
Marshall, J., A. Adcroft, C. Hill, L. Perelman, and C. Heisey (1997), A finite-volume, incompressible Navier Stokes model for studies of the ocean on parallel computers, *J. Geophys. Res.*, *102*(C3), 5753–5766.
Moffat, C. (2014), Wind-driven modulation of warm water supply to a proglacial fjord, Jorge Montt glacier, Patagonia, *Geophys. Res. Lett.*, *41*, 3943–3950, doi:10.1002/2014GL060071.
Morlighem, M., E. Rignot, and J. Willis (2016), Improving bed topography mapping of Greenland glaciers using NASA's oceans melting Greenland (OMG) data, *Oceanography*, *29*(4), 40.
Mortensen, J., K. Lennert, J. Bendtsen, and S. Rysgaard (2011), Heat sources for glacial melt in a sub-Arctic fjord (Godthbsfjord) in contact with the Greenland ice sheet, *J. Geophys. Res.*, *116*, C01013, doi:10.1029/2010JC006528.
Mortensen, J., J. Bendtsen, R. Motyka, K. Lennert, M. Truffer, M. Fahnestock, and S. Rysgaard (2013), On the seasonal freshwater stratification in the proximity of fast-flowing tidewater outlet glaciers in a sub-Arctic sill fjord, *J. Geophys. Res. Oceans*, *118*, 1382–1395, doi:10.1002/jgrc.20134.
Mortensen, J., J. Bendtsen, K. Lennert, and S. Rysgaard (2014), Seasonal variability of the circulation system in a west Greenland tidewater outlet glacier fjord, Godthåbsfjord (64 n), *J. Geophys. Res. Earth Surf.*, *119*, 2591–2603, doi:10.1002/2014JF003267.
Morton, B., G. Taylor, and J. Turner (1956), Turbulent gravitational convection from maintained and instantaneous sources, *Proc. R. Soc. London Ser. A*, *234*(1196), 1–23.
Motyka, R. J., L. Hunter, K. a. Echelmeyer, and C. Connor (2003), Submarine melting at the terminus of a temperate tidewater glacier, Leconte glacier, Alaska, U.S.A., *Ann. Glaciol.*, *36*(1), 57–65.
Motyka, R. J., W. P. Dryer, J. Amundson, M. Truffer, and M. Fahnestock (2013), Rapid submarine melting driven by subglacial discharge, LeConte Glacier, Alaska, *Geophys. Res. Lett.*, *40*, 5153–5158, doi:10.1002/grl.51011.
Nilsen, F., F. Cottier, R. Skogseth, and S. Mattsson (2008), Fjord–shelf exchanges controlled by ice and brine production: The interannual variation of Alantic water in isfjorden, Svalbard, *Cont. Shelf Res.*, *28*(14), 1838–1853.
Padman, L., and S. Erofeeva (2004), A barotropic inverse tidal model for the Arctic Ocean, *Geophys. Res. Lett.*, *31*, L02303, doi:10.1029/2003GL019003.
Pedlosky, J. (1987), *Geophysical Fluid Dynamics*, 2nd edition, Springer-Verlag, New York.
Pickart, R. S., D. J. Torres, and P. S. Fratantoni (2005), The east Greenland spill jet, *J. Phys. Oceanogr.*, *35*(6), 1037–1053.
Qiu, B., N. Imasato, and T. Awaji (1988), Baroclinic instability of buoyancy-driven coastal density currents, *J. Geophys. Res.*, *93*(C5), 5037–5050.
Rignot, E., I. Fenty, Y. Xu, C. Cai, I. Velicogna, C. Ó. Cofaigh, J. Dowdeswell, W. Weinrebe, G. Catania, and D. Duncan (2016), Bathymetry data reveal glaciers vulnerable to ice-ocean interaction in Uummannaq and Vaigat glacial fjords, West Greenland, *Geophys. Res. Lett.*, *43*, 2667–2674, doi:10.1002/2016GL067832.
Sciascia, R., F. Straneo, C. Cenedese, and P. Heimbach (2013), Seasonal variability of submarine melt rate and circulation in an East Greenland fjord, *J. Geophys. Res. Oceans*, *118*, 2492–2506, doi:10.1002/jgrc.20142.

Sciascia, R., C. Cenedese, D. Nicol, P. Heimbach, and F. Straneo (2014), Impact of periodic intermediary flows on submarine melting of a Greenland glacier, *J. Geophys. Res. Oceans*, *119*, 7078–7098, doi:10.1002/2014JC009953.
Slater, D., P. Nienow, A. Sole, T. Cowton, R. Mottram, P. Langen, and D. Mair (2017), Spatially distributed runoff at the grounding line of a large Greenlandic tidewater glacier inferred from plume modelling, *J. Glaciol.*, *63*(238), 309–323.
Slater, D. A., P. W. Nienow, T. R. Cowton, D. N. Goldberg, and A. J. Sole (2015), Effect of near-terminus subglacial hydrology on tidewater glacier submarine melt rates, *Geophys. Res. Lett.*, *42*, 2861–2868, doi:10.1002/2014GL062494.
Slater, D. A., D. N. Goldberg, P. W. Nienow, and T. R. Cowton (2016), Scalings for submarine melting at tidewater glaciers from buoyant plume theory, *J. Phys. Oceanogr.*, *46*(6), 1839–1855.
Speer, K. G. (1989), A forced baroclinic vortex around a hydrothermal plume, *Geophys. Res. Lett.*, *16*(5), 461–464.
Speer, K. G., and J. Marshall (1995a), The growth of convective plumes at seafloor hot springs, *J. Mar. Res.*, *53*(6), 1025–1057.
Speer, K. G., and J. Marshall (1995b), The growth of convective plumes at seafloor hot springs, *J. Mar. Res.*, *53*(6), 1025–1057.
Staalstrøm, A., L. Arneborg, B. Liljebladh, and G. Broström (2015), Observations of turbulence caused by a combination of tides and mean baroclinic flow over a fjord sill, *J. Phys. Oceanogr.*, *45*(2), 355–368.
Stashchuk, N., M. Inall, and V. Vlasenko (2007), Analysis of supercritical stratified tidal flow in a Scottish fjord, *J. Phys. Oceanogr.*, *37*(7), 1793–1810.
Stevens, L. A., F. Straneo, S. B. Das, A. J. Plueddemann, A. L. Kukulya, and M. Morlighem (2016), Linking glacially modified waters to catchment-scale subglacial discharge using autonomous underwater vehicle observations, *Cryosphere*, *10*(1), 417–432.
Stigebrandt, A. (1987), A model for the vertial circulation of the Baltic deep water, *J. Phys. Oceanogr.*, *17*(10), 1772–1785.
Stigebrandt, A. (2012), Hydrodynamics and circulation of fjords, in *Encyclopedia of Lakes and Reservoirs*, edited by L. Bengtsson, R. W. Herschy, and R. W. Fairbridge, pp. 327–344, Spring Science, Dordrecht, Netherlands.
Stigebrandt, A., and J. Aure (1989), Vertical mixing in basin waters of fjords, *J. Phys. Oceanogr.*, *19*(7), 917–926.
Støylen, E., and I. Fer (2014), Tidally induced internal motion in an arctic fjord, *Nonlinear Processes Geophys.*, *21*(1), 87–100.
Støylen, E., and J. E. H. Weber (2010), Mass transport induced by internal kelvin waves beneath shore-fast ice, *J. Geophys. Res.*, *115*, C03022, doi:10.1029/2009JC005298.
Straneo, F., and C. Cenedese (2015), The dynamics of Greenland's glacial fjords and their role in climate, *Annu. Rev. Mar. Sci.*, *7*, 89–112.
Straneo, F., and P. Heimbach (2013), North Atlantic warming and the retreat of Greenland's outlet glaciers, *Nature*, *504*(7478), 36–43.
Straneo, F., G. S. Hamilton, D. A. Sutherland, L. A. Stearns, F. Davidson, M. O. Hammill, G. B. Stenson, and A. Rosing-Asvid (2010), Rapid circulation of warm subtropical waters in a major glacial fjord in East Greenland, *Nature Geoscience*, *3*(3), 182–186.
Straneo, F., R. G. Curry, D. A. Sutherland, G. S. Hamilton, C. Cenedese, K. Våge, and L. A. Stearns (2011), Impact of fjord dynamics and glacial runoff on the circulation near Helheim Glacier, *Nat. Geosci.*, *4*(5), 322–327.
Sulak, D. (2016), Iceberg properties and distributions in three Greenlandic fjords using satellite imagery, Master's thesis, Univ. of Oreg., Eugene, Oregon.
Sulak, D. J., D. A. Sutherland, E. M. Enderlin, L. A. Stearns, and G. S. Hamilton (2017), Iceberg properties and distributions in three Greenlandic fjords using satellite imagery, *Ann. Glaciol.*, 1–15, doi:10.1017/aog.2017.5.
Sutherland, D. A., and F. Straneo (2012), Estimating ocean heat transports and submarine melt rates in Sermilik Fjord, Greenland, using lowered acoustic Doppler current profiler (LADCP) velocity profiles, *Ann. Glaciol.*, *53*(60), 50–58.
Sutherland, D. A., G. E. Roth, G. S. Hamilton, S. H. Mernild, L. A. Stearns, and F. Straneo (2014a), Quantifying flow regimes in a Greenland glacial fjord using iceberg drifters, *Geophys. Res. Lett.*, *41*, 8411–8420, doi:10.1002/2014GL062256.
Sutherland, D. A., F. Straneo, and R. S. Pickart (2014b), Characteristics and dynamics of two major Greenland glacial fjords, *J. Geophys. Res. Oceans*, *119*, 3767–3791, doi:10.1002/2013JC009786.
Svendsen, H., and R. O. Thompson (1978), Wind-driven circulation in a fjord, *J. Phys. Oceanogr.*, *8*(4), 703–712.
Svendsen, H., et al. (2002), The physical environment of kongsfjorden–krossfjorden, an Arctic fjord system in Svalbard, *Polar Res.*, *21*(1), 133–166.
Tseng, Y.-H., F. O. Bryan, and M. M. Whitney (2016), Impacts of the representation of riverine freshwater input in the community earth system model, *Ocean Modell.*, *105*, 71–86.
van den Broeke, M., J. Bamber, J. Ettema, E. Rignot, E. Schrama, W. J. van de Berg, E. van Meijgaard, I. Velicogna, and B. Wouters (2009), Partitioning recent Greenland mass loss, *Science*, *326*(5955), 984–986.
Walters, R. A., E. Josberger, and C. Driedger (1988), Columbia bay, Alaska: An upside down' estuary, *Estuarine Coastal Shelf Sci.*, *26*(6), 607–617.
Xu, Y., E. Rignot, D. Menemenlis, and M. Koppes (2012), Numerical experiments on subaqueous melting of Greenland tidewater glaciers in response to ocean warming and enhanced subglacial discharge, *Ann. Glaciol.*, *53*(60), 229–234.
Xu, Y., E. Rignot, I. Fenty, D. Menemenlis, and M. M. Flexas (2013), Subaqueous melting of Store Glacier, west Greenland from three-dimensional, high-resolution numerical modeling and ocean observations, *Geophys. Res. Lett.*, *40*, 4648–4653, doi:10.1002/grl.50825.